SHmax orientation in the Alpine region from observations of stress-induced anisotropy of nonlinear elasticity

Delorey, Andrew A.
Aiman, Yongki A.
Lu, Yang
Bokelmann, Götz

To be published in: Geophysical Journal International

DOI to publisher's version: 10.1093/gji/ggad353

Geophysical Journal International

Geophys. J. Int. (2023) **235,** 2137–2148
Advance Access publication 2023 September 13
GJI Seismology

https://doi.org/10.1093/gji/ggad353

S_{Hmax} orientation in the Alpine region from observations of stress-induced anisotropy of nonlinear elasticity

Y. A. Aiman,[1] A. A. Delorey,[2] Y. Lu[1] and G. Bokelmann[1]

[1] *Department of Meteorology and Geophysics, University of Vienna, Vienna* 1090, *Austria. E-mail: yongki.aiman@univie.ac.at*
[2] *Geophysics Group, Los Alamos National Laboratory, P.O. Box* 1663, *New Mexico* 87545, *USA*

Accepted 2023 August 28. Received 2023 August 22; in original form 2022 December 19

SUMMARY

The orientation of S_{Hmax} is commonly estimated from *in situ* borehole breakouts and earthquake focal mechanisms. Borehole measurements are expensive, and therefore sparse, and earthquake measurements can only be made in regions with many well-characterized earthquakes. Here, we derive the stress-field orientation using stress-induced anisotropy in nonlinear elasticity. In this method, we measure the strain derivative of velocity as a function of azimuth. We use a natural pump-probe (NPP) approach which consists of measuring elastic wave speed using empirical Green's functions (probe) at different points of the earth tidal strain cycle (pump). The approach is validated using a larger data set in the Northern Alpine Foreland region where the orientation of maximum horizontal compressive stress is known from borehole breakouts and drilling-induced fractures. The technique resolves NNW-SSW to N-S directed S_{Hmax} which is in good agreement with conventional methods and the recent crustal stress model. We confirm that the NPP method can be applied to dense large-scale seismic arrays. The technique is then applied to the Southern Alps to understand the contemporary stress pattern associated with the ongoing deformation due to counterclockwise rotation of the Adriatic plate with respect to the European plate. Our results explain why the two major faults in Northeastern Italy, the Giudicarie Fault and the Periadriatic Line (Pustertal–Gailtal Fault) are currently inactive, while the currently acting stress field allows faults in Slovenia to deform actively. We have demonstrated that the pump-probe method has the potential to fill in the measurement gap left by conventional approaches, both in terms of regional coverage and in depth.

Key words: Coda waves; Seismic interferometry; Seismic noise; Dynamics: seismotectonics; Stress-induced anisotropy; Nonlinear elasticity.

1 INTRODUCTION

The state of stress in the Earth's crust is an important quantity for earth sciences and engineering. A central measure in tectonic stress is the orientation of the maximum horizontal compressive stress (S_{Hmax}). Knowledge of the S_{Hmax} orientation provides many benefits ranging from assisting in designing underground excavations to facilitate in understanding the forces associated with various tectonic activities. At plate scales, it has been widely observed that the orientation of S_{Hmax} is predominantly subparallel to plate motions suggesting that the first-order stress patterns are created by plate boundary forces (Müller *et al.* 1992). At regional scales (100–500 km), the orientation of S_{Hmax} can be controlled by lateral density contrasts due to, for example, gravitational potential (Chai *et al.* 2021). At local scales ($<$ 100 km), deviations from regional- and plate-scale stress patterns may occur due to active faults, induced stress changes, or local density contrasts (Bell 1996; Tingay *et al.* 2006).

In situ measurements of borehole breakouts and earthquake focal mechanisms provide most of the available S_{Hmax} orientations (Ljunggren *et al.* 2003). However, borehole-based methods are point measurements and expensive, while earthquake measurements are limited to seismically active regions that have well-characterized earthquakes. It is thus of great interest to design additional techniques to constrain the stress field in large regions of continental interiors where no measurements are currently available.

1.1 Stress-induced anisotropy in nonlinear elasticity

Rocks are heterogeneous at all scale lengths and they manifest elastic nonlinear behaviour due to the presence of compliant material discontinuities such as grain boundaries, cracks, fractures, joints and faults (Jaeger & Cook 1979). Nonlinear elastic behaviour of rocks can be clearly observed in laboratory experiments that vary applied stresses (Meegan *et al.* 1993; Johnson & McCall 1994). One

can determine the set of higher order elastic constants that describe elastic nonlinear behaviour from measured elastic constants in rock laboratory experiments (Johnson & Rasolofosaon 1996).

Stress-induced anisotropy is also one of the characteristics that is commonly observed in rocks under pressure experiments which can cause the speed of seismic waves to be faster when compressed and slower when extended (Nur & Simmons 1969; Sayers 1988). In the Earth's crust, where deviatoric stress is common, stress will produce an anisotropy of seismic velocity in both granular and cracked rocks. For both cases, the anisotropy results from the stiffening of internal contacts in the direction parallel to the greater compression and closure of cracks whose plane is normal to the greatest compression, respectively. Stress-induced anisotropy in nonlinear elasticity is exhibited by the stress derivative of velocity being faster in the same orientation as the applied stress. This response is observed to be much larger compared to the classical observation of velocity change under applied stress (Delorey *et al.* 2021). Hence, it is preferable to measure anisotropy in nonlinear elasticity regime.

Currently, the established method available for measuring nonlinear response of materials refers to a technique widely used in the field of nonlinear acoustics called dynamic acoustio-elastic testing (DAET, Renaud *et al.* 2009). DAET belongs to a category of pump-probe methods that have existed since at least the 1950s. It employs two dynamic fields, one to disturb the material elasticity (pump) and the other to measure the induced elastic changes (probe) (Riviére *et al.* 2012, and references therein). Recent developments in laboratory studies have allowed to study the elastic nonlinear behaviour of rocks by applying a high-frequency ultrasonic source to the rock sample in addition to the low-frequency vibration and measure the changes in wave velocities of the high-frequency probe wave (Renaud *et al.* 2012). In this manner, we allow rock samples to experience multiple stress–strain conditions in contrast to the application of static loading. In any case, laboratory experiments have shown how rock responds to stress changes. These changes can be observed via changes in seismic properties, especially in seismic velocities and anisotropy.

On a broader scale, observations of changes in seismic velocity in the Earth's crust can be made by applying the same principles as in laboratory experiments. Perturbations to the medium may result from various natural phenomena, for example from solid-earth tides that cause deformation throughout the Earth due to the gravitational attraction of the moon and the sun. One of the advantages of using solid-earth tides as the pump source in a natural 'pump-probe' experiment is that this phenomenon is well known, and can be modelled (Agnew 1996; Sato *et al.* 1984).

Earlier studies of changes in seismic velocity have used active seismic sources generated by a hydraulic vibrator (De Fazio *et al.* 1973), air guns (Reasenberg *et al.* 1974; Leary *et al.* 1979) or piezoelectric transducers (Yukutake *et al.* 1988; Yamamura *et al.* 2003) to excite high-frequency seismic waves in the natural pump-probe (NPP) experiment. In the last two decades, ambient seismic noise has gained increased attention as a tool to characterize the physical properties of the Earth. Noise from oceans waves, wind and human activity allow deriving seismic velocities (Shapiro & Campillo ; Sens-Schönfelder & Wegler 2006; Nishida *et al.* 2009), and this includes the possibility of observing changes in seismic velocity associated with tidal deformation (Takano *et al.* 2014; Hillers *et al.* 2015; Sens-Schönfelder & Eulenfeld 2019; Delorey *et al.* 2021). Most earlier studies are based on observations from a single seismic station (Sens-Schönfelder & Eulenfeld 2019) or a small seismic array (Takano *et al.* 2014; Hillers *et al.* 2015), and few observations have so far been made using large, dense seismic arrays (Delorey *et al.* 2021).

Although it has been successful to observe changes in seismic velocity related to the solid-earth tides within the expected precision, not many studies have discussed the application of such observations. Recently, Delorey *et al.* (2021) have observed changes in seismic velocity associated with solid-earth tides in seismic networks and demonstrated a directional dependence of the fractional velocity change which coincide with the orientation of S_{Hmax} in Oklahoma and New Mexico.

In their study, S_{Hmax} orientation is estimated based on observation of changes in seismic velocity between period of time when the Earth is in compression and time period when the Earth is in extension according to tidal strain pattern. The difference between the two velocities is greatest in the direction of S_{Hmax}.

The purpose of this paper is twofold. First, we test the NPP method (Delorey *et al.* 2021) using a dense large-scale seismic network in the Northern Alpine Foreland region where the orientation of S_{Hmax} is relatively well known from borehole-based measurements. Secondly, we apply the NPP method to the Southern Alps in order to understand the contemporary stress pattern.

1.2 Geology of study area

The study area selected to test the NPP method is the Northern Alpine Foreland region (Fig. 1), a roughly triangular-shape landform stretching from Lake Constance in the west bordering Switzerland, Germany, and Austria to around city of Linz in the east such that the Danube river becomes its upper boundary and the Alps are its lower boundary. The main feature of the Northern Alpine Foreland region is the Molasse Basin (MB), also referred to as the North Alpine Foreland basin, which was formed during the Oligocene and Miocene periods. The MB was formed as a result of the collision between the Adriatic plate and the European plate leading up to the subsidence of transported Alpine nappes (Bachmann & Müller 1992).

Earlier studies have been carried out to characterize the tectonic stress in the Northern Alpine Foreland and surrounding regions using various methods at different scales. For example, the stress patterns for Western Europe are suggested to be oriented NW-SE based on finite-element modelling (Grünthal & Stromeyer 1992) and earlier compilation of the World Stress Map (WSM) database (Müller *et al.* 1992). The WSM is an attempt to compile present-day stress information derived from mostly borehole-based measurements and earthquake focal plane solutions in order to understand the stress state in the Earth's lithosphere (Zoback *et al.* 1989). Recent compilation of the WSM database shows that the second- and third-order stress patterns can have a meaningful influence, causing deviations of stress orientation with respect to the plate-wide stress patterns for certain structurally preferred regions such as in the Northern Alpine Foreland (Heidbach *et al.* 2018; Reinecker *et al.* 2010).

Since the late 1990s, many boreholes have been drilled in this region, providing a wealth of information on stress-field orientation. With the addition of recent data from the MB adjacent to the Alps, Reinecker *et al.* (2010) made an interpretation of borehole breakouts on 67 wells that fell in the A-C quality category based on the assessment description from the WSM project (A is the most reliable and D is the least) to study the relative influence of the Alpine orogen on the European stress pattern (Fig. 1). Reinecker *et al.* (2010) suggested the general pattern of S_{Hmax} is perpendicular to

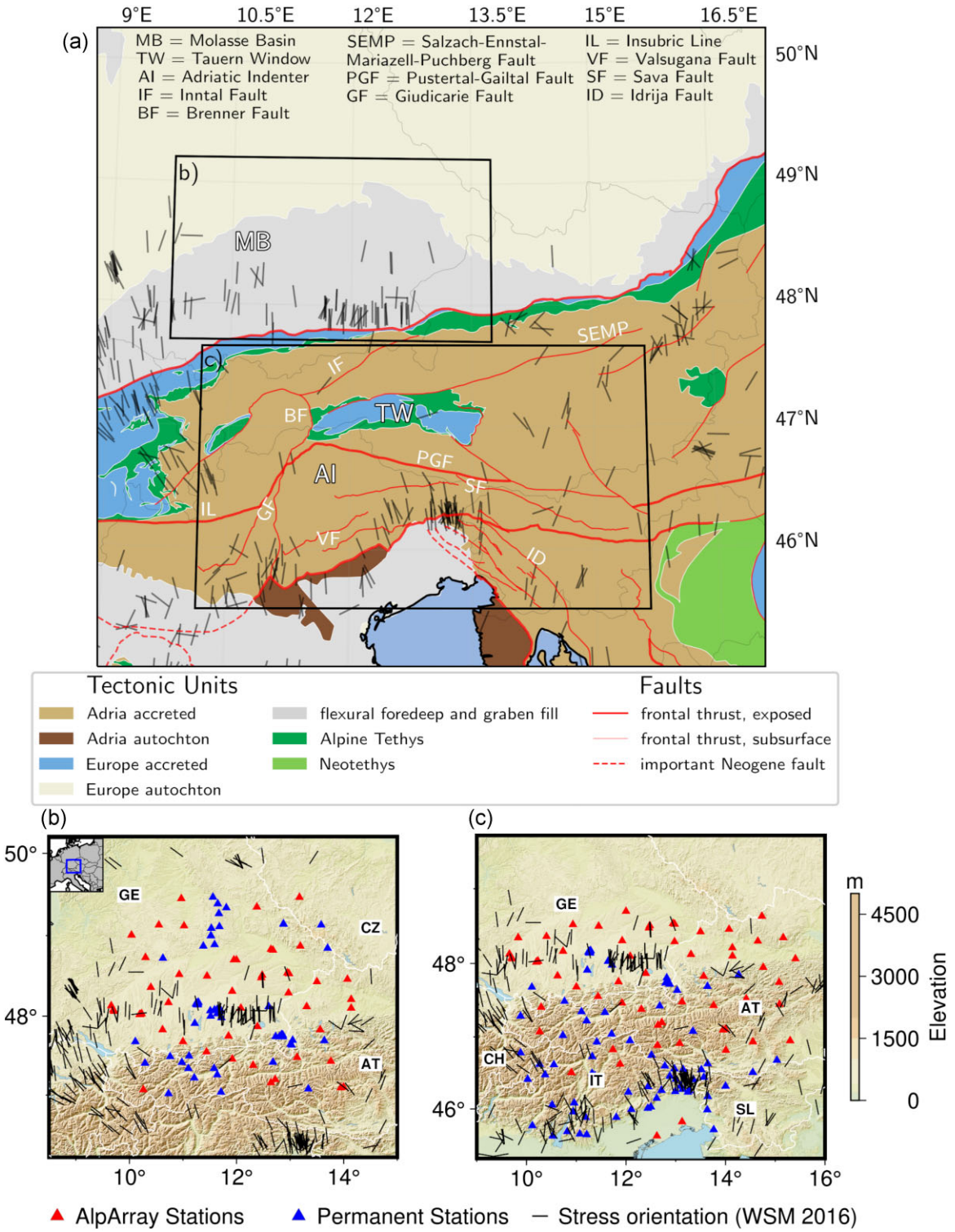

Figure 1. (a) Geological units in the study region (Schmid *et al.* 2004; Handy *et al.* 2010), and stress-field orientation as reported in the WSM database release 2016 (black bars). The bottom shows the seismic station distribution in the Northern Alpine Foreland region as a validation study area (b) and in the Southern Alps as an application study area (c). GE = Germany, CZ = Czech Republic, AT = Austria, CH = Switzerland, IT = Italy and SL = Slovenia.

the strike of the Alpine front (AF) in the near vicinity north of the Alps between Lake Geneva and Salzburg. The abundance of observations of the S_{Hmax} orientation makes the Northern Alpine Foreland a suitable study area to test our method for inferring stress-field orientation.

We apply the NPP method in the Southern Alps, with a focus on the region around the Adriatic Indenter (AI). The AI lies in the northern part of the Adriatic plate that has collided with the European plate leading to complex structure of the Earth's crust and upper mantle beneath the Alps (Ratschbacher *et al.* 1991). The

AI is bounded by the Periadriatic Line or Pustertal–Gailtal Fault (PGF) to the north and by the Giudicarie Fault (GF) to the west which meet to form a corner in the northern part of the AI. To the northeast of the AI is the Tauern Window (TW) of the Eastern Alps, which exposes the lower crust of the European plate (Schmid *et al.* 2004).

Compared to the Northern Alpine Foreland region, higher variability in the stress pattern is observed in the Southern Alps due to complex deformation (Seithel *et al.* 2015; Levi *et al.* 2019). The heterogeneity of the local stress field may result in deviations from the NW-SE directed S_{Hmax} orientation for Western Europe (Müller *et al.* 1992). Local deviations in the area of investigation might be related to the ongoing rotation of the Adriatic Block relative to the European Plate in a counterclockwise direction.

In addition, the selected application area also includes regions with a high level of seismicity. An example of a large and devastating earthquake is the 1976 M_w 6.5 Friuli earthquake. Even though this earthquake sequence has contributed to a rich data set, it is still difficult to understand the stress conditions due to the complex tectonic configuration of this area. Furthermore, faults are known to locally influence the orientation of S_{Hmax} and might provide information regarding which faults are active and which are expected to rupture in the future. The two major faults that form the tip of the AI, the PGF and the GF, should accommodate large deformations. However, seismic hazard maps and seismicity data show that the area around these two faults has lower hazard and less seismicity compared to other faults in the surrounding area (Fig. 2). There is a regional gap in stress measurement in the Alps. Thus, understanding the contemporary stress pattern by means of the NPP method is of great interest in this region.

In this study, we infer S_{Hmax} orientations in the Northern Alpine Foreland region and the Southern Alps based on analysing seismic velocity changes associated with solid-earth tides. We explain the data and method used in our study in Section 2 and present the results in Section 3. After, we discuss in more details what we observed in our results in Section 4. What motivates our study, beside testing this new technique, is to understand why some of the most important faults in the Alps, especially the PGF and the Giudiucarie fault, are not seismically active in recent times (Fig. 2), while minor faults in the same general area are active. We aim to determine if the new stress field measurements can help us to understand this.

2 DATA AND METHOD

2.1 Seismic data

For the validation study area in the Northern Alpine Foreland region, we used the vertical component of ambient seismic noise data from 2016 to 2018 recorded at 58 permanent seismic stations [CZ: Czech Regional Seismic Network (1973); GR: German Regional Seismic Network (1976); OE: Austrian Seismic Network (1987); BW: BayernNetz (2001)] and 53 temporary seismic stations (Z3: AlpArray seismic network 2015). For the application study area in the Southern Alps, we used the vertical component of ambient seismic noise data from 2016 to 2019 recorded at 77 permanent seismic stations [CZ network; GR network; OE network; BW network; ST: Trentino Seismic Network (1981); CH: Switzerland Seismological Network (1983); IV: Italian National Seismic Network (2005); SL: Seismic Network of the Republic of Slovenia (1990); NI: North-East Italy Broadband Network (2002); SI: Province Südtirol (2006); OX: North-East Italy Seismic Network (2016)] and 60 temporary AlpArray seismic stations.

The two data sets were pre-processed in the same manner, starting with detrending, removing instrument response, downsampling to 2 Hz and then storing the data in an hourly basis. We eliminated recorded earthquake signals and performed time-domain normalization on the data in a similar way as Boué *et al.* (2014) and Lu *et al.* (2018). Earthquake signals are removed based on the energy ratio between two chunks of hourly cross-correlation functions (CCFs) and the influence of transient signals are reduced based on the median value of the absolute amplitude of the trace.

After all pre-processing stages were completed, cross correlations were calculated on an hourly basis over a period ranging from ∼3 to 10 s (0.1–0.3 Hz). We keep the cross-correlated waveforms in hourly format because the method we use to infer the stress-field orientation relies on clustering our collection of 1-hr CCFs according to the strain patterns represented by modelled solid-earth tides data over the same period of observation.

We performed data selection by examining the overall CCF that emerged after applying the stacking procedure for all hourly CCFs for each station pair. As we will employ the early coda wave in the NPP method, we expect a well-defined Rayleigh wave part of the overall CCF and also a clear decay in amplitude immediately after the Rayleigh wave train characterizing the coda part of the overall CCF. For each interstation overall CCF, we applied three different quality control criteria. The first criteria defined as the signal-to-noise (SNR) ratio of the maximum amplitude of the overall CCF to the precursor signal that comes before the Rayleigh wave. The second criteria is defined as the SNR of the maximum amplitude of the overall CCF to the trailing background noise. The third criteria is defined as the ratio of the maximum amplitude of the signal to the earlier part of the coda wave. These data selection procedure helped us to obtain the expected coda wave, resulting in reliable and high-quality list of station pairs that will be required to cluster our hourly CCFs associated with periods of high (extensional) and low (compressional) strain.

2.2 'Natural' pump-probe method

We have estimated the volumetric strain due to Earth tides in the study area using the software package SPOTL (Agnew 1996). The SPOTL program is mainly used to calculate ocean-tide loading. For our purpose, the approximated solid-earth tides are computed based on a defining tidal forcing series generated by external bodies for a location and combining it with the response of the Earth to tides. Considering the limited spatial variations observed in the solid-earth tidal deformation pattern across the study area (see Fig. S1, Supporting Information), we chose to utilize results derived from the central location to represent this pattern. The resulting time-series pattern, as shown in Fig. 3, is used as a reference to determine time windows when the Earth is experiencing high strain (extension) and time windows when the Earth is in low-strain period (compression). We divided hourly CCFs into two groups based on tidal strain magnitude where the top 25 per cent refers to extension and the bottom 25 per cent refers to compression. We then calculated overall CCF stacks for all station pairs associated with the extension and compression groups.

The early coda part of the resulting compressional and extensional CCF stacks are extracted by defining the starting time of the coda window as 2.5 times the estimated arrival time of the Rayleigh wave with duration of 30 s (Fig. 4). In order to maintain quality

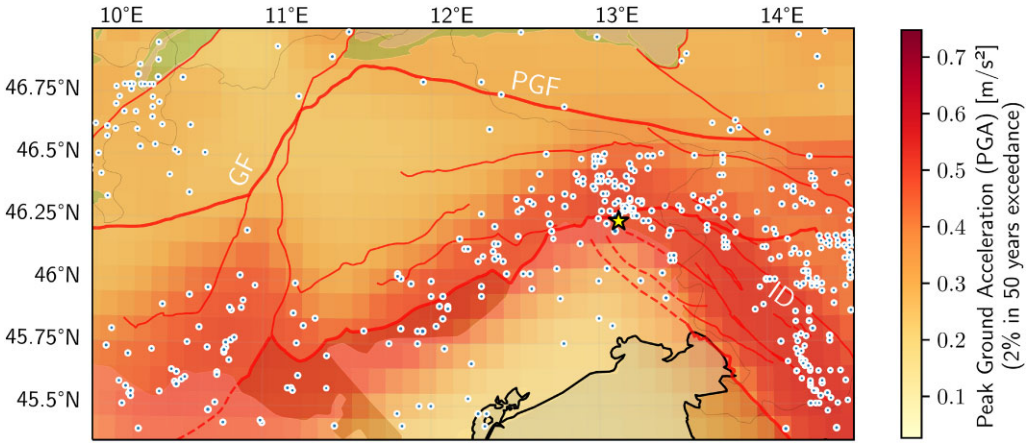

Figure 2. Seismic hazard, seismicity and major faults (e.g. PGF = Pustertal-Gailtal Fault; GF = Giudicarie Fault and ID = Idrija Fault) in the Southern Alps (Danciu *et al.* 2021) indicate low hazard and less seismicity in the region around the GF and the PGF, in contrast to the region around the ID where higher hazard and more seismicity is observed. The yellow star represents the location of the 1976 M_w 6.5 Friuli earthquake.

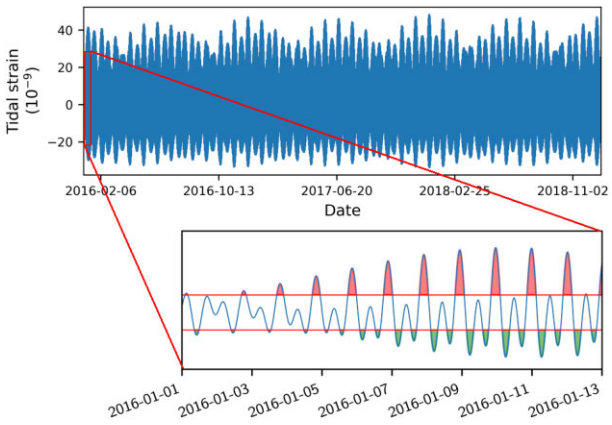

Figure 3. Tidal solid-earth deformation from 2016 to 2019 obtained from the SPOTL package. These predictions are used as reference to select inter-station hourly CCFs associated with periods of high (extensional) and low (compressional) strain.

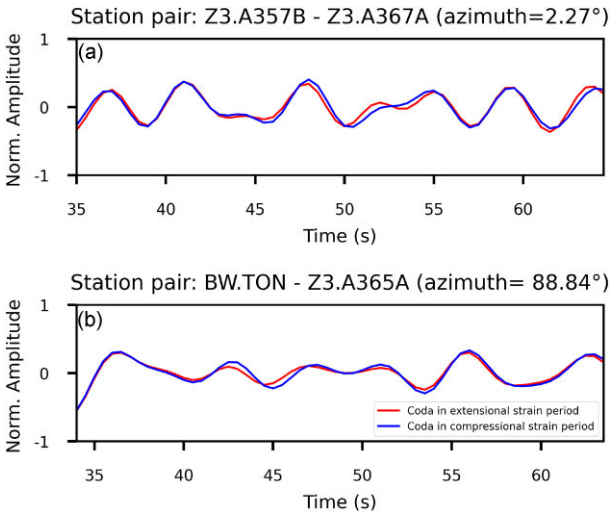

Figure 4. An example of 30 s time window of the earlier coda of the stack over all individual CCFs. We calculated the time difference between coda in compressional strain period (blue) and coda in extensional strain period (red) using the so-called wavelet method (Mao *et al.* 2020) to infer relative velocity change.

of the data after the division into extension group and compression group, we applied data selection by calculating the correlation coefficient between overall CCF from the extension group and overall CCF from the compression group for each station pair. We only consider station pairs that have correlation coefficient values above 0.9. We measured the relative velocity changes between coda waves from the compression group and coda waves from the extension group using the wavelet method (Mao *et al.* 2020). This technique can provide optimal time–frequency joint resolution and allows us to accurately estimate the dv/v variations at discrete frequencies. In this study, we analysed coda waves around 5 s period because we expect the Rayleigh wave part contained in coda waves to be sensitive to the top few kilometres in the subsurface (Obermann *et al.* 2013).

After calculating the relative seismic velocity changes using the wavelet method for all station pairs, we associated the dv/v values to the azimuth of each station pair in order to examine directional dependence of relative velocity changes. In this study, a station pair oriented N-S is indicated by azimuth of 0° or 180°, while azimuth of 90° refers to the E-W direction. We eliminate outliers in our dv/v collection by excluding dv/v values that are greater than 3 times the standard deviation of the dv/v collection. We calculated average values of dv/v every 6°. The resulting azimuthal dependence is then smoothed via a Gaussian kernel.

3 RESULTS

3.1 Azimuthal dependence of relative velocity change

We estimated the orientation of S_{Hmax} based on the sine function that best fits the distribution of the dv/v values with respect to the azimuth of station pairs. The relative change in velocity between the compression and the extension periods can serve as a proxy for the stress derivative of the seismic velocity with respect to strain (called nonlinear seismic velocity susceptibility) observed in NPP experiment (Delorey *et al.* 2021). The maximum value of nonlinear seismic velocity susceptibility should coincide with the orientation of S_{Hmax} which is the maximum (negative) magnitude of the best-fitting sine curve.

As a validation test, we calculated the orientation of S_{Hmax} throughout the northern Alpine Foreland region using a wave period of 5 s, which resulted in an orientation of S_{Hmax} of 164.8°. This is

in a good agreement with the average orientation of S_{Hmax} derived by conventional methods in WSM database (Fig. 5a). Furthermore, we conducted additional tests to investigate whether there exists a time delay in velocity changes relative to tidal deformation. This is achieved by shifting the time windows used for grouping hourly CCFs for the compression and extension regimes. The results, presented in Fig. S2 (Supporting Information), revealed an interesting finding: a potential time delay of approximately 30 min. This observation could be utilized to optimize our approach, such as refining the grouping of compression and extension regimes. The detailed mechanism behind this time delay warrants further investigation and extends beyond the scope of our current study. It is important to emphasize, however, that despite the time delay, the inferred orientation of S_{Hmax} remains consistent, indicating a similar pattern of NNW-SSE to N-S. We then applied our approach to infer the overall orientation of S_{Hmax} for the Southern Alps region (Fig. 5b). Interpretation of the S_{Hmax} orientation inferred from our approach and its comparison with the S_{Hmax} orientation from conventional methods will be provided in Section 4.

3.2 Spatial distribution of S_{Hmax} orientation

We created a spatial distribution of S_{Hmax} orientations by dividing the investigation area into several circular grid cells with a radius of ∼0.5°. We consider station pairs that lie within a search radius of 1.25° for the Northern Alpine Foreland region and 0.75° for the Southern Alps region and estimated the orientation of S_{Hmax} with the method described in Section 2.2 providing 8 × 6 grid cells for the Northern Alpine Foreland region and 9 × 5 grid cells for the Southern Alps region (Fig. 6). Each centre of the circular grid of cells represents the orientation of S_{Hmax} of the surrounding area.

To compare the regionalized S_{Hmax} orientations derived from ambient seismic noise data with individual S_{Hmax} orientations obtained from the borehole-based measurements or earthquake focal mechanism methods, we calculated the difference between the S_{Hmax} orientation of each grid cell and any S_{Hmax} orientation from WSM database that lies in the same circular grid cell within the validation test study area, the Northern Alpine Foreland region. We presented the differences as histogram in Fig. 6(a).

4 DISCUSSION

4.1 S_{Hmax} orientation inferred from ambient seismic noise for the Northern Alpine Foreland region

In Section 3.1, we have shown that the NPP method can infer the S_{Hmax} orientation by utilizing a dense, large-scale seismic network. The overall S_{Hmax} pattern for the Northern Alpine Foreland region derived by the NPP method indicates NNW-SSE direction which is in good agreement with the S_{Hmax} orientation provided by the WSM database (black bars in Fig. 6a). Comparatively small differences in determining the exact S_{Hmax} orientation might be attributed to the relative importance of the forces acting on a region. For Western Europe, the first-order forces, that is, the resistive forces due to the collision between the Eurasian and African plate and ridge-push forces associated with the Mid-Atlantic ridge, are considered to influence the stress pattern resulting an average of S_{Hmax} orientation of 144° (Müller *et al.* 1992; Heidbach *et al.* 2007). On the other hand, most of the borehole measurements in the MB adjacent to the Alps show N-S directed S_{Hmax}. This indicates that the stress pattern is controlled by the gravitational potential energy generated by Alpine topography rather than plate boundary forces (Reinecker *et al.* 2010). In our case, the NPP method estimates the S_{Hmax} orientation in the region within the seismic array. This places our inferred S_{Hmax} orientation for the Northern Alpine Foreland in between the influence of plate boundary forces and gravitational potential energy due to Alpine topography.

We estimated the regionalized S_{Hmax} orientations for the Northern Alpine Foreland region by defining a grid of cells representing smaller scale S_{Hmax} orientations. In general, the inferred S_{Hmax} orientations based on the NPP method are consistent with the individual S_{Hmax} orientations from the WSM database as shown in histogram in Fig. 6(a). We defined three levels of uncertainty in our measurements based on standard deviation of phase estimates of best-fitting parameters, dark red represents low uncertainty (< 10°), red represents medium level of uncertainty (10°–30°) and light red represents high uncertainty (> 30°). S_{Hmax} orientations with high and medium uncertainty values are generally found on the periphery of the study area. This could be due to the lack of available station pairs resulting in fewer measurement points and some azimuthal gaps. In addition, it is possible that the estimated S_{Hmax} orientation with greater uncertainty comes from measurement points with complex geological conditions. We provided the matrix density plots for individual S_{Hmax} orientations and azimuth uncertainties for all gridpoints for the Northern Alpine Foreland region in the Supporting Information (Fig. S3).

In the central part of the study area, close to many available borehole measurements, S_{Hmax} orientations estimated from the NPP method shows NNW-SSE rather than N-S as shown by the WSM database. The N-S trend indicates a strong influence of the gravitational potential energy of the Alpine topography compared to the plate boundary forces (Reinecker *et al.* 2010). We do not observe this trend for the individual measurements around the frontal part of the Alps. This might be due to the contribution from neighbouring station pairs that sample some parts of the Alps where the stress field is more heterogeneous. To the east, where there are no borehole-based measurements or focal plane solutions available, our method estimates N-S S_{Hmax} orientations which are perpendicular to the AF. A small group of individual measurements in the northeastern part of the Northern Alpine Foreland study area share the same S_{Hmax} orientation, that is, NNE-SSW deviated from the general trend when entering the Bohemian Massif region (Heidbach *et al.* 2007; Schippkus *et al.* 2020). Interpreting the S_{Hmax} orientations for the western part of the study area is more difficult due to a higher uncertainty in the measurements. Regionally perturbed stress patterns in the eastern Swiss MB and the eastern Jura Mountains have been observed, likely due to the influence of the Black Forest Massif and the change of the strike of the AF resulting in dominant WNW-ESE S_{Hmax} orientation (Becker 2000).

We have selected six individual measurements located around a region where borehole-based measurements are widely available (blue box in Fig. 6a). In this subregion, there are at least 42 borehole-based S_{Hmax} orientation measurements registered in the WSM database with average depth of ∼2 km and a maximum depth of 4.16 km. The general pattern of S_{Hmax} orientations in this subregion is N-S ranging from 171° to 13°. Nevertheless, there are six WSM measurements that deviate from the N-S trend in this subregion, showing an NE-SW to E-W directed S_{Hmax} orientation. Our result shows, in general, the NNW-SSE directed S_{Hmax} orientation for the same subregion. For each measurement within this subregion, the calculated relative velocity changes with respect to the azimuth of station pairs are provided in the Supporting Information (Fig. S5).

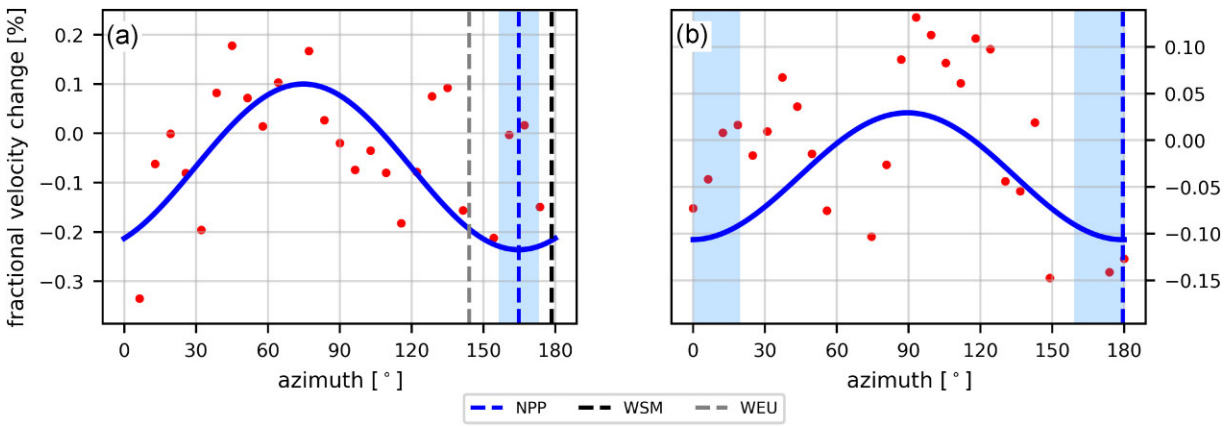

Figure 5. Relative velocity change (red dots) with respect to the azimuth of station pairs in (a) the Northern Alpine Foreland region and (b) the Southern Alps. The blue line shows the best-fitting sine function for each study area. The inferred S_{Hmax} orientation from the NPP method is indicated by a dashed blue line with the standard deviation of the phase estimates of the sine wave fitted to the relative velocity changes (blue region). It is compared to the average of S_{Hmax} orientation derived from the WSM database (dashed black line) and the average of S_{Hmax} orientation for Western Europe (dashed grey line) for the validation study area.

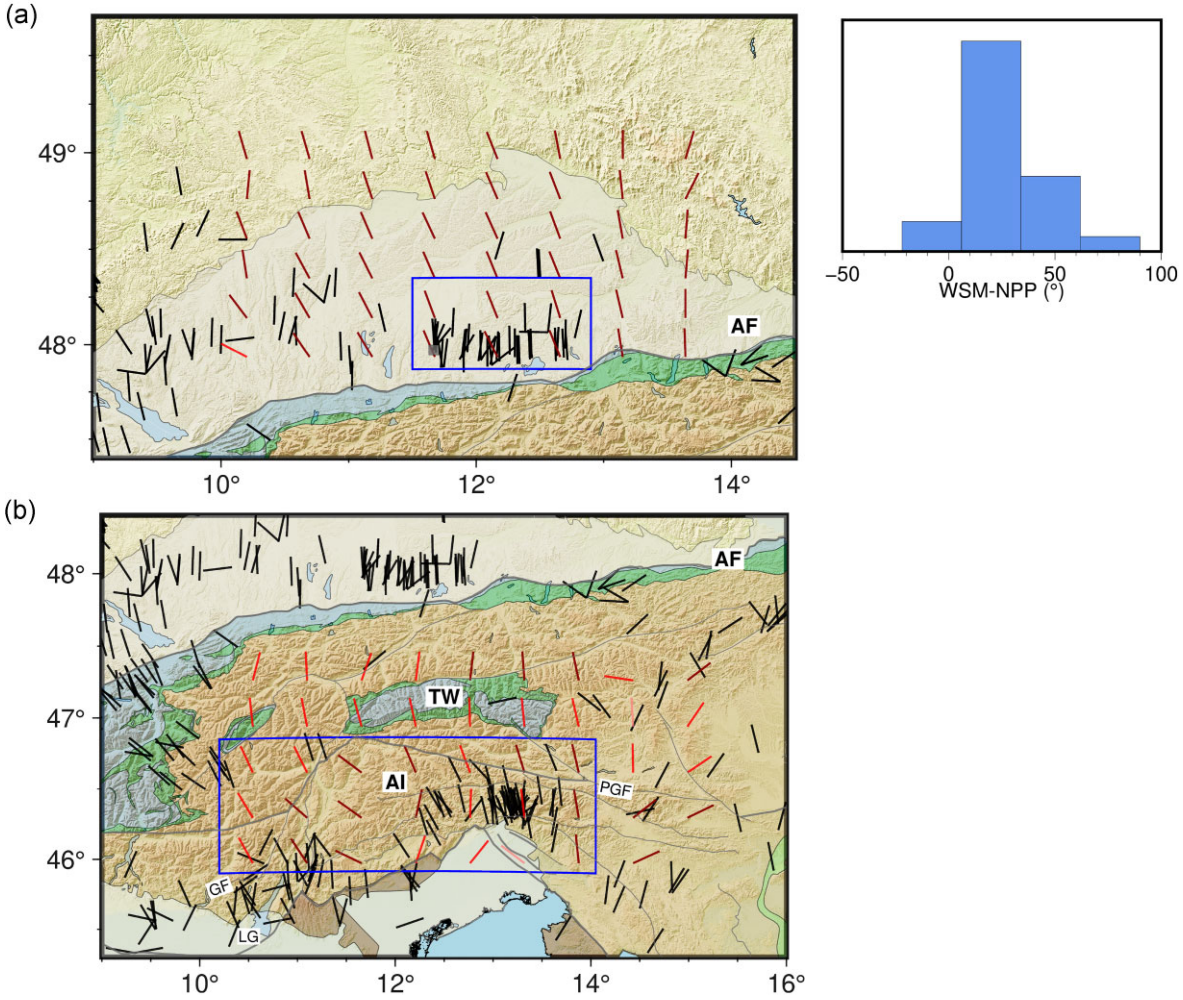

Figure 6. Regionalized orientation of S_{Hmax} (red bars; darker red indicates S_{Hmax} orientation with low uncertainty, while lighter red represents S_{Hmax} orientation with higher uncertainty) compared to the S_{Hmax} orientation compiled by the WSM database (black bars) for (a) the Northern Alpine Foreland region and (b) the Southern Alps. The histogram on the top right of (a) shows the differences between the two data sets indicating both approaches are in good agreement. Subregions are defined for a detailed comparison in Section 4 (blue rectangle). Grey lines indicate faults. A small grey box represents the location of the Sauerlach geothermal site. Tectonic units, faults and related surface feature are displayed as follow: AF, TW, AI, GF, PGF and LG.

Prior studies have used a variety of approaches to infer the stress conditions in the earth's crust in the Northern Alpine Foreland region, particularly in the MB. Reinecker *et al.* (2010) highlighted the localized variations of S_{Hmax} orientation that deviate from the N-S trend within the German MB region that might be due to the presence of active faults nearby or difficulties interpreting large drilling-induced fractures as breakouts on log data. Seithel *et al.* (2015) focused on the Sauerlach site (SE of Munich city; around the southwestern part of the subregion) which consists of three greatly deviated wells (Th1, Th2 and Th3 in Seithel *et al.* 2015) and reported a local stress anomaly based on the interpretation of stress indicators and fracture sets. The *in situ* stress interpretation was made by transforming the regional stress field into the local coordinate system of the wellbore and comparing the observed orientations to the modelled stress orientations. By allowing the variation of stress regime in the calculation, Seithel *et al.* (2015) concluded local stress changes are observed in the vicinity of the wells. One model scenario proposed for well Th1 allows the modelled stress orientations to fit the observed orientations if the S_{Hmax} orientation is 140°–150° in a strike-slip regime, which is in a good agreement with the S_{Hmax} orientation derived from our approach. The discussion about the stress regime in the Northern Alpine Foreland region is provided in the Supporting Information.

The NNW-SSE S_{Hmax} orientation estimated by our method fits the crustal stress pattern of Germany based on finite-element modelling taking into account the differentiation of sedimentary layers (Ahlers *et al.* 2022). This model of S_{Hmax} orientation is calculated based on the assumption of linear elasticity. They compared this model with the mean orientation of S_{Hmax} derived from the WSM database and additional data provided by Levi *et al.* (2019). The mean orientation of S_{Hmax} is calculated on a 0.5×0.5 grid, considering at least 10 data records within a search radius of 200 km. For a subset of the region around the Northern Alpine Foreland, the modelled S_{Hmax} orientation also shows general NNW-SSE trend, which is in a good agreement with the S_{Hmax} orientation inferred from our method. Furthermore, the angular deviation between the modelled S_{Hmax} orientation by Ahlers *et al.* (2022) and the mean orientation from the WSM database and additional data by Levi *et al.* (2019) shows a range of differences similar to that obtained by our method (shown as histogram in Fig. 6a).

4.2 S_{Hmax} orientation inferred from ambient seismic noise for the Southern Alpine region

In the previous section, we have confirmed that the NPP method can be applied on a large scale to resolve the present-day S_{Hmax} orientation in the Northern Alpine Foreland region. The same procedure has been applied to the Southern Alps.

We divided the investigation area into 9×5 circular grids and estimated the orientation of the S_{Hmax} at each grid centre considering the available station pairs within a radius of 55 km from the grid centre. We defined uncertainties for individual S_{Hmax} orientations based on criteria described in Section 4.1 and provided the matrix density plot in the Supporting Information (Fig. S4). It is worth mentioning that in this application we reduce the search radius of available station pairs within one grid cell in order to avoid averaging over too large a scale. In general, the inferred S_{Hmax} orientations show the N-S trend which corresponds to the expected relative motion of the Adria microplate with respect to Europe.

In particular, we elaborate on our observations and compare them with previous studies for the region defined by the blue box in Fig. 6(b). This subregion includes the area around the GF system in the western part of the AI and the seismically active Veneto-Friuli area in the eastern part of the AI. Around the Northern GF, the S_{Hmax} orientations derived from our measurement indicate NW-SE to NNW-SSE orientation, while the WSM database shows no data in that area, and a high variability of S_{Hmax} orientations (between NNW-SSE and NE-SW) further South, around the northeast of Lake Garda (LG). Most of the S_{Hmax} orientations provided by the WSM database are derived from earthquake focal mechanisms. There are only two borehole measurements indicating N-S orientation to the east of LG, however, they are located in the Po Plain region. Vigano *et al.* (2008) and Reiter *et al.* (2018) made separate interpretations based on a stress analysis of earthquake focal mechanisms confirming our observation of the NW-SE to NNW-SSE directed S_{Hmax} for this area. For the eastern part of the AI, the S_{Hmax} orientations inferred from our method show NNW-SSE to N-S orientations which are in good agreement with denser observation provided by the WSM database. This trend is also supported by separate analysis of fault plane solutions by Reiter *et al.* (2018) which indicates NNW-SSE oriented S_{Hmax} in the Eastern Periadriatic Fault System. Our measurements also capture a clockwise rotation from NW-SE oriented S_{Hmax} in the southwestern area of investigation to N-S oriented S_{Hmax} in the centre, which is in agreement with the results from the earthquake focal mechanisms (Reiter *et al.* 2018).

The observation of stress orientation might provide some understanding about the degree of activity in the seismotectonic region. Here, we highlight our observation of the S_{Hmax} orientation for several seismotectonic regions in the Southern Alps (Fig. 7):

(i) Northern Giudicarie

The western part of the AI is characterized by the GF system, a left-lateral displacement that has had a total displacement of about 70 km (Prosser 1998). It was active during late Oligocene-early Miocene. Our results suggest that the S_{Hmax} is oriented nearly perpendicularly on the fault. Under that stress field, the Northern GF can not be active presently. Indeed, there are no indications that it currently is, as shown in the seismic hazard map in Fig. 2. When it was active, during the Giudicarie phase about 15 Ma, the S_{Hmax} was orientated 100°–110° (Martin *et al.* 1998), rather than the currently approximated 140°. Further south there is a large set of earthquakes, with a great diversity of focal mechanisms (Saraò *et al.* 2021), and this is reflected in the WSM (see Fig. 7). Our results suggest that the regionally averaged stress field is similar to the one further north. Across the Northern GF, there is a slight change in average orientation of S_{Hmax}, and similarly in internal deformation (Sánchez *et al.* 2018). This contrast goes beyond the scope of this paper.

(ii) Friuli

The region of the 1976 M_w 6.5 Friuli earthquake, at longitude 13°E and latitude 46.5°N, is of particular interest. We have shown that both our method and the WSM database show mostly N-S oriented S_{Hmax} indicating the shortening direction. To the west, there is a rotation of the stress field to smaller angles which is consistent with the geometry of faults in the region as well as seismicity (Burrato *et al.* 2008). At longitude 12°E and to the west of it, there is a paucity of seismicity during the last decades, yet this region is of much interest for seismic hazard analysis, since larger earthquakes are expected in that area (Burrato *et al.* 2008).

(iii) Periadriatic fault (PGF)

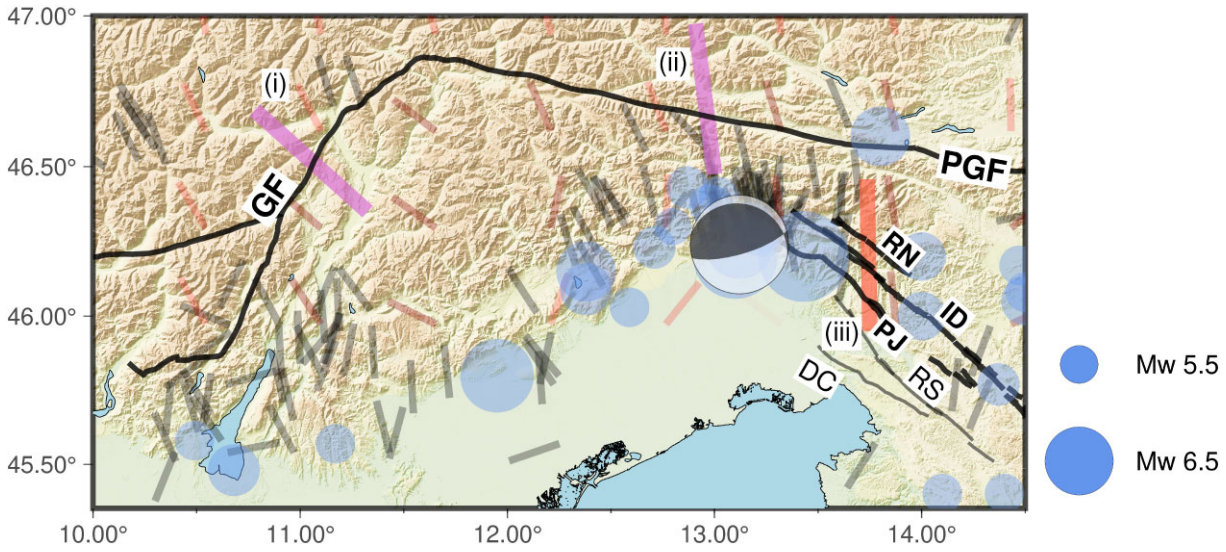

Figure 7. The average orientation of the S_{Hmax} (large magenta bars and orange bar) estimated from the WSM database (short black bars) and this study (short red bars) around the major strike-slip faults (thick black lines) in the Southern Alps which correspond to the degree of seismicity: (i) the orientation of the S_{Hmax} is nearly perpendicular (∼80°) to the orientation of the GF indicating the fault should not be active, (ii) the orientation of the S_{Hmax} is different from the orientation of the PGF (∼72°), (iii) the angle between S_{Hmax} orientation and the orientation of the Dinaric Fault System [Ravne Fault (RN), Idrija Fault (ID) and Predjama Fault (PJ)] is favourable for slip (∼48°). A focal mechanism for the 1976 M_w 6.5 Friuli earthquake is shown.

The Periadriatic fault is a major fault with past dextral motion (Schmid *et al.* 1989). Our results suggest that the maximum compressive stress orientation is currently not far from the fault normal (about 20° difference) in the region which we consider (10–14°E), and this small angle probably renders current or future activation unlikely. Indeed, there are essentially no signs of any current activity (Saraò *et al.* 2021, Fig. 2).

(iv) Slovenia

In the east of our study region (Western Slovenia), there is a set of parallel transcurrent faults, for example, the Ravne, Idrija, Predjama, Raša and Divača fault (Vičič *et al.* 2019). A more comprehensive picture of the faults in the area is given by Atanackov *et al.* (2021). In any case, the faults are essentially parallel to each other, with a strike direction that is roughly NW-SE. The sense of deformation on the faults is dextral strike-slip. Our results suggest that S_{Hmax} is mostly oriented near N-S. Angles between the faults and S_{Hmax} are therefore near 45°. Shear stresses acting on the faults are therefore maximum, and it is not a surprise that there is active deformation on some of these faults.

4.3 Measurement gaps in determining S_{Hmax} orientation

The orientation of S_{Hmax} is commonly inferred either from various borehole-based methods or by inverting earthquake focal mechanism. These available methods suffer from measurement gaps in both depth and spatial resolution. In the Northern Alpine Foreland region, the WSM database shows the distribution of the earthquakes occur between 6–11 km in depth and the mean depth of various borehole methods is approximately 2 km. This depth discrepancy of the inferred S_{Hmax} orientations among conventional methods is important to discuss because it might show a complexity of the stress state at the Earth's crust. One prominent examples is the S_{Hmax} orientations in the Jura mountain region, especially around the southern Upper Rhine Graben, where fault-plane solutions and 10 *in situ* measurements indicate a ∼30° counterclockwise rotation of S_{Hmax} orientation with depth (Becker 2000). Most of the earthquakes used to infer S_{Hmax} orientation in this region originate from depth range between 5 and 15 km with maximum depth of 30 km. The determination of S_{Hmax} orientation using scattered Rayleigh waves with a period of 5 s, based on nonlinear susceptibility of seismic wave velocities, is sensitive to the upper ∼5 km, and may fill this measurement gap (Obermann *et al.* 2013).

In addition, the S_{Hmax} orientations derived from conventional methods are not evenly distributed. They are only available in the region where boreholes are available and earthquakes occur. Resolving the global stress pattern of the Earth's crust is important. One approach to understand the global crustal stress pattern can be achieved by smoothing the stress field, derived from earthquake focal mechanisms and borehole-based measurements, and calculating the average of S_{Hmax} orientations on a regular grid (Heidbach *et al.* 2018). Although neighbouring individual data records may indicate high variability of S_{Hmax} orientations, smoothing process can serve as a long-wavelength filter that suppresses local variations in stress-field orientation. Heidbach *et al.* (2018) have shown the global crustal stress pattern can be obtained based on S_{Hmax} orientation using fixed search radius of $r = 500$ km for 2° grid. It is worth noting that the calculated mean S_{Hmax} orientations do not necessarily reflect the S_{Hmax} orientation at the gridpoints. Local deviations can be hidden due to the use of such a large search radius. The regionalized S_{Hmax} orientation inferred from ambient seismic noise may resolve the global stress pattern of the Earth's crust at a range of scales as it can be applied in regions where there are insufficient earthquake or borehole observations.

4.4 Effect of poroelasticity

Fig. 5 shows the azimuthal dependence of relative velocity changes (dv/v). We may categorize the dv/v values into two regimes based on the sign of the value. In our method, the overall CCF from the compression group serve as the reference waveforms when calculating relative velocity changes, while the overall CCF from the

extension group serve as the current/perturbed waveforms. As a consequence, a negative *dv*/*v* value is associated with an increase in seismic velocity due to compression or a decrease in seismic velocity due to extension. This can be interpreted as the opening/closing of cracks in the Earth's crust caused by solid-earth tides. In contrary, an increase in seismic velocity during periods of extension or a decrease during periods of compression would produce a positive *dv*/*v* value. This reverse phenomenon can be caused by various factors, but the most likely one is due to the effect of poroelasticity that often observed in the Earth's crust. It is widely accepted that many locations in Earth's crust can be considered a fluid-saturated poroelastic medium (Roeloffs 1996). This has become an interesting topic for discussion, especially in relation to earthquake hydrology and natural phenomena that can induce aftershocks. This supports the argument that fluid pressure is important at the depths where earthquakes occur, hence the concept of poroelasticity should be considered in addition to effective elasticity in order to explain most phenomena that occur in the Earth's crust. In our case, the poroelasticity has contributed to the relative velocity changes in both areas of investigation indicated by the azimuthal dependence of *dv*/*v* moving towards the positive regime.

The influence of poroelasticity on seismic velocity change measurements has been widely observed. Silver *et al.* (2007) conducted *in situ* measurements of temporal variations in seismic velocity at two test sites using an active source. The results show a strong and positive correlation with barometric pressure change at one test site and, on the other hand, a significant negative correlation with barometric pressure for another site. They interpreted their positive and negative correlations as the influence of near- and far-field effects of the stress dependence in a poroelastic medium. In addition to the active source experiment, laboratory rock experiments by vibrating rock samples at low frequencies in order to cycle them through different stress–strain levels show similar behaviour in sedimentary rock samples (Renaud *et al.* 2012). Fontainebleau sandstone exhibits nonlinear elasticity anomaly behaviour which is indicated by a very large positive value of the quadratic nonlinear elastic coefficient obtained from the experiment, meaning that the speed of sound decreases during axial compressive strain. Although it is not discussed in detail what could cause this effect, measurements of certain rock types have shown the possibility that seismic velocities in rocks may decrease during periods of compression. Another observation is shown by *in situ* measurements of velocity changes in response to tidal deformation using ambient seismic noise recordings (Hillers *et al.* 2015). Measurements on vertical correlation component indicate reduced wave speeds during periods of volumetric compression. They interpreted their observations to be related to the dilatant effect on the porous rock.

5 CONCLUSIONS

We have inferred the orientation of the maximum horizontal compressive stress (S_{Hmax}) from stress-induced anisotropy in nonlinear elasticity using ambient seismic noise data in the Northern Alpine Foreland region and Southern Alps. The homogeneous NNW-SSE directed S_{Hmax} observed in the Northern Alpine Foreland region from the NPP experiment fits the recent high-resolution crustal stress field model and is in good agreement with the observed S_{Hmax} orientations derived from borehole-based methods and earthquake focal mechanisms. In addition, we also showed that our approach can be applied to the Southern Alps where the state of the stress is less well known, and more complex. Our results indicate that the S_{Hmax} orientation rotates from NW-SE in the southwest of Southern Alps to N-S to the east of the Southern Alps. Furthermore, we have demonstrated that inferred stress orientations from ambient seismic noise can be useful for regional seismotectonic analysis, and they can address questions as to which faults are active, and which are not.

The pump-probe approach complements conventional methods of determining the S_{Hmax} orientation. It reflects S_{Hmax} orientation measurements in the upper ∼5 km which can fill the observation gap that has so far been obtained from borehole-based methods (up to 1–2 km depth from earth surface) and earthquake focal mechanisms (>5 km depth). It has advantages over conventional methods since noise-based studies can be applied in regions where there are no earthquakes and/or boreholes.

ACKNOWLEDGMENT

We would like to thank the operators of the seismic networks who make their data available through the EIDA (http://www.orfeus-eu.org/eida). We also thank the two anonymous reviewers for their insightful remarks that helped in improving this manuscript.

DATA AVAILABILITY

The seismic waveform data used in this paper are available through the European Integrated Data Archive (EIDA; http://www.orfeus-eu.org/data/eida/).

REFERENCES

Agnew, D. C., 1996. *SPOTL: Some Programs for Ocean-tide Loading, SIO Ref. Ser. 96–8,* p. 35, Scripps Institution of Oceanography, La Jolla, CA.

Ahlers, S. *et al.*, 2022. The crustal stress field of Germany: a refined prediction, *Geotherm. Energy,* **10,** 10 , doi:10.1186/s40517-022-00222-6.

Atanackov, J. *et al.*, 2021. Database of active faults in Slovenia: compiling a new active fault database at the junction between the Alps, the Dinarides and the Pannonian Basin Tectonic Domains, *Front. Earth Sci.,* **9** , doi:10.3389/feart.2021.604388.

Bachmann, G. H. & Müller, M., 1992. Sedimentary and structural evolution of the German Molasse Basin, *Eclogae geol. Helv.,* **85**(3), 519–530.

Bachmann, G. H., Müller, M. & Weggen, K., 1987. Evolution of the Molasse Basin (Germany, Switzerland), *Tectonophysics,* **137**(1–4), 77–92.

Becker, A., 2000. The Jura Mountains—an active Foreland fold-and-thrust belt?, *Tectonophysics,* **321**(4), 381–406.

Bell, J. S., 1996a. In situ stresses in sedimentary rocks (Part 2): applications of stress measurements, *Geosci. Can.,* **23,** 135–153.

Boué, P., Roux, P., Campillo, M. & Briand, X., 2014. Phase velocity tomography of surface waves using ambient noise cross correlation and array processing, *J. geophys. Res.: Solid Earth,* **119**(1), 519–529.

Burrato, P., Poli, M. E., Vannoli, P., Zanferrari, A., Basili, R. & Galadini, F., 2008. Sources of Mw 5+ earthquakes in northeastern Italy and western Slovenia: an updated view based on geological and seismological evidence, *Tectonophysics,* **453**(1–4), 157–176.

BW: BayernNetz, 2001. *Department of Earth and Environmental Sciences, Geophysical Observatory,* University of Munchen, [Data set], International Federation of Digital Seismograph Networks , doi:10.7914/SN/BW.

CH: Switzerland Seismological Network, 1983. *CH: Swiss Seismological Service (SED) At ETH Zurich,* National Seismic Networks of Switzerland, ETH Zürich , doi:10.12686/sed/networks/ch.

Chai, C., *et al.*, 2021. A 3D full stress tensor model for Oklahoma, *J. geophys. Res.: Solid Earth,* **126,** e2020JB021113, d oi:10.1029/2020JB021113.

CZ network; GR network; OE network; BW network; ST: Trentino Seismic Network, 1981. *Geological Survey-Provincia Autonoma di Trento,*

Trentino Seismic Network [Data set], International Federation of Digital Seismograph Networks , doi:10.7914/SN/ST.

CZ: Czech Regional Seismic Network, 1973. *CZ: Charles University in Prague (Czech),* Institute of Geonics, Institute of Geophysics, Academy of Sciences of the Czech Republic, Institute of Physics of the Earth Masaryk University (Czech), and Institute of Rock Structure and Mechanics, Czech Regional Seismic Network [Data set], International Federation of Digital Seismograph Networks , doi:10.7914/SN/CZ.

Danciu, L. *et al.*, 2021. *The 2020 update of the European Seismic Hazard Model: Model Overview,* EFEHR Technical Report 001, v1.0.0 , doi:10.12686/a15.

De Fazio, T. L., Aki, K. & Alba, J., 1973. Solid earth tide and observed change in the in situ seismic velocity, *J. geophys. Res.,* **78**(8), 1319–1322.

Delorey, A.A., Bokelmann, G.H.R., Johnson, C.W. & Johnson, P.A., 2021. Estimation of the orientation of stress in the Earth's crust without earthquake or borehole data, *Commun. Earth Environ.,* **2,** 190 , doi:10.1038/s43247-021-00244-1.

GR: German Regional Seismic Network, 1976. *GR: Federal Institute for Geosciences and Natural Resources,* German Regional Seismic Network (GRSN), Bundesanstalt für Geowissenschaften und Rohstoffe , doi:10.25928/mbx6-hr74.

Grünthal, G. & Stromeyer, D., 1992. The recent crustal stress field in Central Europe: trajectories and finite element modelling, *J. geophys. Res.,* **97**(B8), 11.805–11.820.

Handy, M., Schmid, S., Bousquet, R., Kissling, E. & Bernoulli, D., 2010. Reconciling plate-tectonic recon-structions of Alpine Tethys with the geological–geophysical record of spreading and subduction in the Alps, *Earth Sci. Rev.,* **102,** 121–158.

Heidbach, O., Reinecker, J., Tingay, M., Müler, B., Sperner, B., Fuchs, K. & Wenzel, F., 2007. Plate boundary forces are not enough: second- and third-order stress patterns highlighted in the World Stress Map database, *Tectonics,* **26,** TC6014 , doi:10.1029/2007TC002133.

Heidbach, O *et al.*, 2018. The World Stress Map database release 2016: crustal stress pattern across scales, *Tectonophysics,* **744,** 484–498.

Hillers, G., Retailleau, L., Campillo, M., Inbal, A., Ampuero, J.-P. & Nishimura, T., 2015. In situ observations of velocity changes in response to tidal deformation from analysis of the high-frequency ambient wavefield, *J. geophys. Res. Solid Earth,* **120,** 210–225.

Illies, J., Baumann, H. & Hoffers, B., 1981. Stress pattern and strain release in the Alpine Foreland, in *Developments in Geotectonics,* Vol. **16,** pp. 157–172, Elsevier , doi:10.1016/B978-0-444-41953-8.50024-4.

Illies, J. & Greiner, G., 1978. Rhinegraben and the Alpine system, *GSA Bull.,* **89**(5), 770–782.

IV: Italian National Seismic Network, 2005. *Istituto Nazionale di Geofisica e Vulcanologia (INGV),* Rete Sismica Nazionale (RSN), Istituto Nazionale di Geofisica e Vulcanologia (INGV) , doi:10.13127/SD/X0FXnH7QfY.

Jaeger, J. & Cook, N., 1979. *Fundamentals of Rock Mechanics, 3rd edition,* Chapman and Hall, ISBN 0 412 22010 5.

Johnson, P. A. & McCall, K. R., 1994. Observation and implications of nonlinear elastic wave response in rock, *Geophys. Res. Lett.,* **21**(3), 165–168.

Johnson, P. A. & Rasolofosaon, P. N. J., 1996. Nonlinear elasticity and stress-induced anisotropy in rock., *J. geophys. Res.,* **101,** 3113–3124.

Kraemer, C., 2009. *Identifikation hotizontaler Blattverschiebungen im Untergrund des Molassetrogs - neue Interpretationsergebnisse auf Grundlage von 2D-Seismik,* Paper presented at the Geothermiekongress, Germany, Bochum.

Leary, P. C., Malin, P. E., Phinney, R. A., Brocher, T. & VonColln, R., 1979. Systematic monitoring of millisecond travel time variations near Palmdale, California, *J. geophys. Res.,* **84**(B2), 659–666.

Levi, N., Habermueller, M., Exner, U., Piani, E., Wiesmayr, G. & Decker, K., 2019. The stress field in the frontal part of the Eastern Alps (Austria) from borehole image log data, *Tectonophysics,* **769,** 228175 , doi:10.1016/j.tecto.2019.228175.

Ljunggren, C., Chang, Y., Janson, T. & Christiansson, R., 2003. An overview of rock stress measurement methods, *Int. J. Rock Mech. Min. Sci.,* **40,** 975–989.

Lu, Y., Stehly, L., Paul, A. & AlpArray Working Group, 2018. High-resolution surface wave tomography of the European crust and uppermost mantle from ambient seismic noise, *J. geophys. Int.,* **214**(2), 1136–1150.

Mao, S., Mordret, A., Campillo, M., Fang, H. & van der Hilst, R., 2020. On the measurement of seismic traveltime changes in the time–frequency domain with wavelet cross-spectrum analysis, *J. geophys. Int.,* **221**(1), 550–568.

Martin, S., Bigazzi, G., Zattin, M., Viola, G. & Balestrieri, M., 1998. Neogene kinematics of the Giudicarie fault (Central-Eastern Alps, Italy): new apatite fission-track data, *Terra Nova,* **10,** 217–221.

Meegan, G. D., Johnson, P., Guyer, R. & McCall, K., 1993. Observations of nonlinear elastic wave behavior in sandstone, *J. acoust. Soc. Am.,* **94**(6), 3387–3391.

Megies, T. & Wassermann, J., 2014. Microseismicity observed at a non-pressure-stimulated geothermal power plant, *Geothermics,* **52,** 36–49.

Mueller, M., Nieberding, F. & Wanninger, A., 1988. Tectonic style and pressure distribution at the Northern Margin of the Alps between Lake Constance and the River Inn, *Geol. Rundsch.,* **77**(3), 787–96.

Müler, B., Zoback, M.L., Fuchs, K., Mastin, L., Gregersen, S., Pavoni, N., Stephansson, O. & Ljunggren, C., 1992. Regional patterns of tectonic stress in Europe, *J. geophys. Res.,* **97,** 11783–11803.

NI: North-East Italy Broadband Network, 2002. *OGS (Istituto Nazionale di Oceanografia e di Geofisica Sperimentale) and University of Trieste,* North-East Italy Broadband Network [Data set], International Federation of Digital Seismograph Networks , doi:10.7914/SN/NI.

Nishida, K., Montagner, J. P. & Kawakatsu, H., 2009. Global surface wave tomography using seismic hum, *Science,* **326**(5949), 112 , doi:10.1126/science.1176389.

Nur, A. & Simmons, G., 1969. Stress-induced velocity anisotropy in rock: an experimental study, *J. geophys. Res.,* **74,** 6667–6674.

Obermann, A., Planès, T., Larose, E., Sens-Schönfelder, C. & Campillo, M., 2013. Depth sensitivity of seismic coda waves to velocity perturbations in an elastic heterogeneous medium, *Geophys. J. Int.,* **194**(1), 372–382.

OE: Austrian Seismic Network, 1987. *OE: ZAMG - Zentralanstalt für Meterologie und Geodynamik,* Austrian Seismic Network [Data set], International Federation of Digital Seismograph Networks , doi:10.7914/SN/OE.

OX: North-East Italy Seismic Network, 2016. *OX: Istituto Nazionale di Oceanografia e di Geofisica Sperimentale - OGS,* North-East Italy Seismic Network [Data set], FDSN , doi:10.7914/SN/OX.

Prosser, G., 1998. Strike-slip movements and thrusting along a transpressive fault zone: the North Giudicarie line (Insubric line, northern Italy), *Tectonics,* **17**(6), 921–937.

Ratschbacher, L., Frisch, W., Linzer, H.-G. & Merle, O., 1991. Lateral extrusion in the eastern Alps, Part 2: structural analysis, *Tectonics,* **10**(2), 257–271.

Reasenberg, P. & Aki, K., 1974. A precise, continuous measurement of seismic velocity for monitoring in situ stress, *J. geophys. Res.,* **79**(2), 399–406.

Reinecker, J., Tingay, M., Müller, B. & Heidbach, O., 2010. Present-day stress orientation in the Molasse Basin, *Tectonophysics,* **482**(1–4), 129–138.

Reiter, F., Freudenthaler, C., Hausmann, H., Ortner, H., Lenhardt, W. & Brandner, R., 2018. Active seismotectonic deformation in front of the Dolomites indenter, Eastern Alps, *Tectonics,* **37,** 4625–4654.

Renaud, G., Callé, S. & Defontaine, M., 2009. Remote dynamic acoustoelastic testing: Elastic and dissipative acoustic nonlinearities measured under hydrostatic tension and compression, *Appl. Phys. Lett.,* **94,** 011905, doi:10.1063/1.30641372258.

Renaud, G., Le Bas, P.-Y. & Johnson, P. A., 2012. Revealing highly complex elastic nonlinear (anelastic) behavior of Earth materials applying a new probe: dynamic acoustoelastic testing, *J. geophys. Res.,* **117,** B06202 , doi:10.1029/2011JB009127.

Riviére, J., Renaud, G., Guyer, R.A. & Johnson, P.A., 2013. Pump and probe waves in dynamic acousto-elasticity: Comprehensive description and comparison with nonlinear elastic theories, *J. appl. Phys.,* **114,** 054905 , doi:10.1063/1.4816395.

Roeloffs, E., 1996. Poroelastic techniques in the study of earthquake-related hydrologic phenomena, *Adv. Geophys.,* **37,** 135–195.

Sánchez, L., Völksen, C., Sokolov, A., Arenz, H. & Seitz, F., 2018. Present-day surface deformation of the Alpine region inferred from geodetic techniques, *Earth Syst. Sci. Data,* **10**(3), 1503–1526.

Saraò, M., Bressan, G., Renner, G. & Restivo, A., 2021. A focal mechanism catalogue of earthquakes that occurred in the southeastern Alps and surrounding areas from 1928–2019, *Earth Syst. Sci. Data,* **13,** 2245–2258.

Sato, T. & Hanada, H., 1984. A program for the computation of oceanic tidal loading effects 'GOTIC', *Publ. Int. Latit. Obs. Mizusawa,* **18,** 29–47.

Sayers, C.M., 1988. Stress-induced ultrasonic wave velocity anisotropy in fractured rock, *Ultrasonics,* **26,** 311–317.

Schippkus, S., Zigone, D. & Bokelmann, G., the AlpArray Working Group, 2020. Azimuthal anisotropy in the wider Vienna basin region: a proxy for the present-day stress field and deformation, *J. geophys. Int.,* **220**(3), 2056–2067.

Schmid, S. M., Aebli, H.R., Heller, F. & Zingg, A., 1989. The role of the Periadriatic Line in the tectonic evolution of the Alps, *Geol. Soc. Lond. Spec. Publ.,* **45,** 135–171.

Schmid, S.M., Fúgenschuh, B., Kissling, E. & Schuster, R., 2004. Tectonic map and overall architecture of the Alpine orogen, *Eclogae geol. Helv.,* **97,** 93–117.

Seithel, R., Steiner, U., Müler, B., Hecht, C. & Kohl, T., 2015. Local stress anomaly in the Bavarian Molasse Basin, *Geotherm. Energy,* **3,** 4 , doi:10.1186/s40517-014-0023-z.

Sens-Schönfelder, C. & Eulenfeld, T., 2019. Probing the in situ elastic nonlinearity of rocks with earth tides and seismic noise, *Phys. Rev. Lett.,* **122**(13), 138501–138506.

Sens-Schönfelder, C. & Wegler, U., 2006. Passive image interferometry and seasonal variations of seismic velocities at Merapi Volcano, Indonesia, *Geophys. Res. Lett.,* **33,** L21302 , doi:10.1029/2006GL027797.

SI: Province Südtirol, 2006. *Province Súdtirol Seismic Network,* Operated by ZAMG – Central Institute for Meteorology and Geodynamics.

Silver, P. G., Daley, T. M., Niu, F. & Majer, E. L., 2007. Active source monitoring of cross-well seismic travel time for stress-induced changes, *Bull. seism. Soc. Am.,* **97**(1B), 281–293.

SL: Seismic Network of the Republic of Slovenia, 1990. *Slovenian Environment Agency,* Seismic Network of the Republic of Slovenia [Data set], International Federation of Digital Seismograph Networks, doi:10.7914/SN/SL.

Takano, T., Nishimura, T., Nakahara, H., Ohta, Y. & Tanaka, S., 2014. Seismic velocity changes caused by the Earth tide: ambient noise correlation analyses of small-array data, *Geophys. Res. Lett.,* **41,** 6131–6136.

Tingay, M., Müller, B., Reinecker, J. & Heidbach, O. 2006. State and origin of the present-day stress field in sedimentary basins: New results from the World Stress Map Project, paper presented at Golden Rocks 2006, in *The 41st U. S. Symposium on Rock Mechanics (USRMS): 50 Years of Rock Mechanics— Landmarks and Future Challenges,* Am. Rock Mech. Assoc., Golden, Colo.

Unger, H-J., 1999. Die Tektonischen Strukturen der bayerischen Ostmolasse, *Documenta Naturae,* **124,** 1–16.

Vičič, B., Aoudia, A., Javed, F., Foroutan, M. & Costa, G., 2019. Geometry and mechanics of the active fault system in western Slovenia, *J. geophys. Int.,* **217**(3), 1755–1766.

Viganò, A., Bressan, G., Ranalli, G. & Martin, S., 2008. Focal mechanism inversion in the Giudicarie–Lessini seismotectonic region (Southern Alps, Italy): insights on tectonic stress and strain, *Tectonophysics,* **460**(1), 106–115.

Yamamura, K., Sano, O., Utada, H., Takei, Y., Nakao, S. & Fukao, Y., 2003. Long-term observation of in situ seismic velocity and attenuation, *J. geophys. Res.,* **108**(B6), 2317 , doi:10.1029/2002JB002005.

Yukutake, H., Nakajima, T. & Doi, K., 1988. In situ measurements of elastic wave velocity in a mine, and the effects of water and stress on their variation, *Tectonophysics,* **149**(1–2), 165–175.

Z3: AlpArray seismic network, 2015. *AlpArray Seismic Network,* AlpArray Seismic Network (AASN) temporary component, AlpArray Working Group , doi:10.12686/alparray/z3_2015.

Ziegler, P. A., 1987. Compressional intra-plate deformation in the Alpine Foreland—an introduction, *Tectonophysics,* **137,** 1–5.

Zoback, M. *et al.*, 1989. Global patterns of tectonic stress, *Nature,* **341,** 291–298.

SUPPORTING INFORMATION

Supplementary data are available at *GJI* online.

suppl_data

Please note: Oxford University Press is not responsible for the content or functionality of any supporting materials supplied by the authors. Any queries (other than missing material) should be directed to the corresponding author for the paper.